Simulation-Based Analysis of Thermally-Induced Stress Effects on Buried-Core Square Waveguide

Yassir Benahjiba, African Leadership Academy
Youssef Nassar, African Leadership Academy

Abstract

The objective of this study was to understand and visualize the effects of thermally-induced stresses resulting from high-temperature manufacturing processes (thermal annealing) on the performance of the buried-core square silicon waveguide. In order to do so, the photoelastic effect, which relates principle stresses and refractive indices, and its impacts were analyzed and investigated. The analysis was performed in COMSOL Multiphysics, utilizing the Finite Element Method (FEM) for numerical calculations. The equivalent stress distribution and strains in the waveguide were determined by exploiting the plane strain assumption. The anisotropic stress distribution in the waveguide caused a change in the refractive indices along the principle axes, causing a change in birefringence. Due to birefringence, optical power density distribution in different modes has experienced variations. However, in higher modes, the variation was more evident as mode splits were exhibited alongside higher optical power confinement, noting that higher confinement is advantageous for low-loss optical waveguides. Thus, it was inferred that the effect of anisotropic stresses was more substantial on higher modes rather than fundamental modes. Finally, it was evident that the mechanical properties of the cladding and manufacturing conditions could be optimized to control birefringence and subsequent performance-governing parameters.

Keywords: Silicon Waveguide, Stress, Photoelastic Effect, Birefringence, COMSOL Multiphysics

1. Introduction

As a result of the increasing demand for high data transmission speeds and high-end information processing beyond the capabilities of conventional electronic platforms, a wide range of optical interconnects, namely Waveguides, have been developed. Waveguides are characterized by their invulnerability against induced crosstalk (undesired data interference) and electromagnetic interference, reaching bandwidths higher than 1 Tb/s and speeds exceeding 10 Gb/s, which are otherwise unachievable via copper-based interconnects [1]. Hence, a complete optical computation and information processing would eliminate the need for optoelectronic conversion, which limits speed and bandwidth along with being power-consuming. In optical circuits, waveguides are akin to the building blocks, enabling low-loss wave propagation.

Generally, the simplest form of waveguides are planar waveguides, which are structured from three layers: lower cladding, core, and upper cladding. Both the cladding layers should have a lower refractive index to confine the propagating light by Total Internal Reflection (TIR) [2]. There have been a wide range of materials used for photonic devices, ranging from fibers to semiconductors, but, currently, the most promising material platform for photonics technology is Silicon for the upcoming era of computational technologies.

Silicon has been, since the mid 20th century, the foundation for the electronics industry, accordingly, billions of dollars and decades of research have been invested in silicon semiconductor device manufacturing. Thus, silicon photonics has emerged as an attempt to apply the Complementary Metal-Oxide Semiconductor (CMOS) process in the

manufacturing of silicon photonic devices, utilizing the already existent platform of silicon electronics [3]. Combining the different functions of different silicon photonic devices, analogously to electronic Integrated Circuits (IC), creates so-called Photonic Integrated Circuits (PIC). The start of silicon photonics was in 1987 [4], which described how injecting carriers in silicon causes material properties, namely refractive index n and k. Accordingly, integrating a PN junction enabled the creation of the first building block of a PIC, a phase modulator [5]. For a long time, silicon photonics has offered the opportunity for miniaturization and monolithic integration with the pre-existent electronic platform. However, a number of challenges have been introduced by the fabrication process, due to its non-conservative nature, of silicon waveguides, mainly birefringence.

The fabrication process of silicon waveguides is highly temperature- dependent, for it utilizes thermal annealing as an integral part of the process [6]. As a result, strains across the waveguide structure are manifested, both intrinsic and stress-induced, due to the non-conservative fabrication processes being used and the thermal mismatching between waveguide layers due to dissimilar thermo-mechanical properties [6]. Thus, birefringence is induced, which is a phenomenon exhibited in optical waveguides, causing a difference in data stream speeds along the waveguide axis, leading to data losses and signal distortion [7]. Two main schemes have been proposed to control birefringence, either by optimizing the waveguide's geometry or stresses applied on the waveguide (stress engineering) [8]. However, due to difficulties faced with the former method and its impracticality with the waveguide being analyzed, stress engineering is the most widely used approach for that waveguide. Stress engineering utilizes the photoelastic effect, which relates the anisotropic stresses and optical properties of material [9], to control the birefringence of the waveguide and, subsequently, device performance [8].

2. Methodology

For understanding and visualizing the photoelastic effect in the waveguide and the impacts of thermally-induced stresses, an isolated single-mode buried-core square waveguide, introduced in [6], is analyzed using COMSOL Multiphysics. After the annealing at a high temperature (1000 °C), a mismatch in the thermal expansion coefficient of waveguide layers imposes a thermally induced stress in the waveguide structure amid operation. That stress is determined utilizing the plane strain approximation and visualized using the von Mises equivalent stress. Due to the photoelastic effect (causing the stress-induced change in refractive indices [9]), anisotropic stress on the waveguide affected the optical properties of propagating waves in the waveguide structure, and ultimately, device performance. Under the photoelastic effect, performance-governing parameters are determined, including electric field power density distribution, the shift in refractive indices, and birefringence. Finally, It should be made clear that no portion of this paper is written by generative AI or any LLM.

3. Theory of Waveguides

3.1. Phase & Polarization

To understand the theory of guided waves, some fundamentals should be illustrated, beginning with the Phase. Light is an optical wave plotted as a function of time; when regarding a function of time, phase is the interval of a periodic waveform that passes a reference point, after time t. An optical wave could be represented, in this example, as a sinusoidal function $sin\theta$, where θ is the phase of this waveform. Alternatively, the wave could be plotted as $sin\omega t$, where ω is a constant indicating angular speed such that ωt is the phase of the function. Generally, the propagating optical wave is represented as [2]:

$$E = E_0 \exp\left[j(kz \pm \omega t)\right] \quad (1)$$

However, under some simplifications, the sinusoidal form of the function could be used:

$$E = E_0 \sin(kz \pm \omega t) \quad (2)$$

In this sinusoidal form, ωt is the phase and the term kz describes the progress of the wave in the z direction.

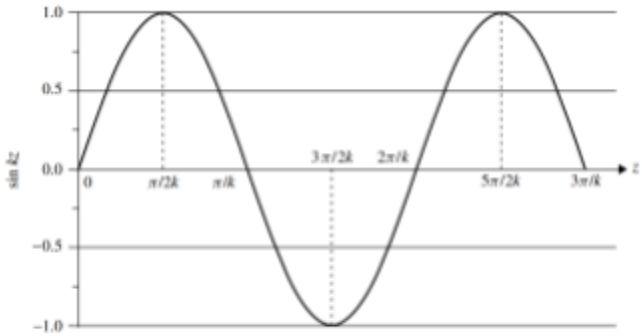

Figure 1: plot of sin *kz*

From the plot of *sinkz* shown in Figure 1, the wavelength λ is defined as follows:

$$\lambda = \frac{2\pi}{k} \tag{3}$$

Since axis interception occurs every $\frac{\pi}{k}$ rather than every π radian, the unit of *k* is radians per meter, determining the magnitude of phase change per meter of propagation distance. Thus, *k* could be, using Equation 3, defined as *wave number* [2]:

$$k = \frac{2\pi}{\lambda} \tag{4}$$

In photonic circuits, it is desired to measure and control the phase of propagating waves, but if it was with respect to time, waves with the same initial time point will have a similar phase. Therefore, it was essential to define the phase change as a function of propagation distance instead:

$$\phi = kz \tag{5}$$

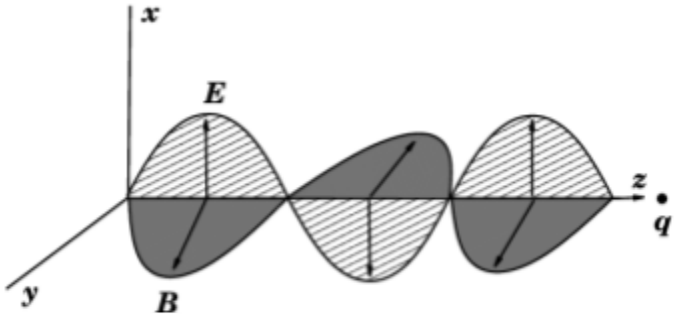

Figure 2: sinusoidal transverse light wave

Due to the transverse nature of the light wave, it has both the characteristics of electric and magnetic fields, varying with time, which could be represented as a simple sinusoidal plane wave as in Figure 2.

In the above figure, a light wave is a plane one as both the electric field (E) and magnetic field (B) is constant through the z plane. The wave is *transverse* as both the two fields are transverse to the direction of the propagation. The wave is also said to be polarised because each field exists in a single direction, where this wave is polarised in x direction as the electric fields solely exist in x direction, meaning that polarization is, by definition, the direction of the electric field of a propagating wave [2]. Light may be polarised in different configurations, including plane, circular, and elliptical polarisation exhibited in Figure 3.

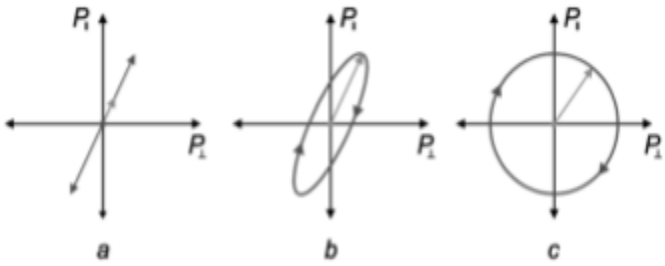

Figure 3: different polarisation configurations traced by electric field

However, in some cases, light could be unpolarised, meaning that electric field vectors are randomly oriented. In optical circuits, plane polarisation is the most desired form as in optical waveguides. Light mostly propagates in plane polarised modes in arbitrary angles, which could be resolved into parallel and perpendicular to waveguide surface [2]. Nonetheless, these two components might propagate in the device with dissimilar properties, causing differently polarised lights to possess different characteristics.

3.2. Ray Optics Approach

Due to the electromagnetic nature of light waves, Maxwell's equations are typically involved when analyzing waveguides. Nevertheless, Maxwell's equations are not needed for all applications, and a much simpler model, *Ray Optics Model*, could be used in understanding simple optical waveguides, dealing with light waves as 2-dimensional straight lines.

Considering the interface between two media of different refractive indices (n_1 and n_2) illustrated in Figure 4. In the medium of refractive index n_1, a light ray (E_i) impinges on the interface between the two media with an angle θ_1. As a result, E_i is partially reflected (E_r) and partially transmitted (E_t).

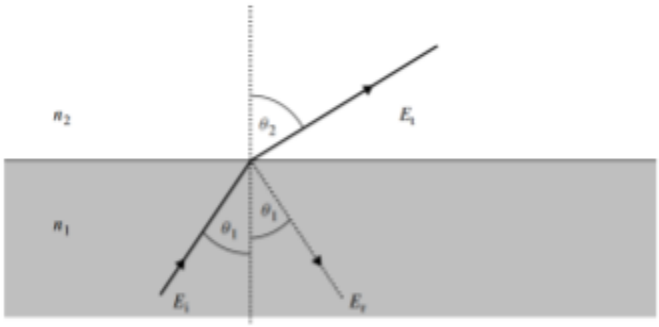

Figure 4: Incident light partially transmitted and reflected at the interface between two media

The relation between refractive indices, angle of incidence, and angle of refraction are governed by *Snell's law* [2]:

$$n_1 \sin\theta_1 = n_2 \sin\theta_2 \tag{6}$$

Observing Figure 4, since θ_2 is clearly greater than θ_1, n_2 is lower than n_1. Thus, as θ_1 increases, at some angle θ_1, θ_2 will be π rad, simplifying Snell's law to:

$$n_1 \sin\theta_1 = n_2 \tag{7}$$

From Equation 7, the critical angle θ_c could be defined as:

$$\theta_c = \sin^{-1}\frac{n_2}{n_1} \tag{8}$$

Intuitively, for incidence angles greater than the critical angle, no light will be transmitted, and Total Internal Reflection (TIR) is manifested, shown in Figure 5. In that sense, light could propagate infinitely if it was confined in a media of higher refractive index than surrounding media if only it was incident at an angle greater than the critical angle. Nevertheless, these two conditions are not sufficient to support light propagation in the waveguide structure [2] as it will be evident in the subsequent sections.

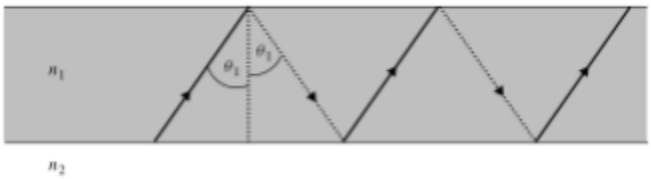

Figure 5: total internal reflection between two interfaces

Enhancing the ray optics model, partial reflection and transmission could be rigorously defined using *Fresnel formulae* to describe reflected and transmitted waves. For instance, the reflected wave (E_r) will have a complex amplitude related to the complex amplitude of the incident wave (E_i) by a complex reflection coefficient:

$$E_r = rE_i \tag{9}$$

where *r* is the complex reflection coefficient; defined by the polarisation of light and incidence angle. Since light waves are transverse electromagnet waves (TEM), there exist two cases in which either the magnetic field or electric field is perpendicular to the plane of incidence (the plane that contains wave normal).

In the *Transverse Electric* (TE) condition, the electric field vector is perpendicular to the incidence plane as depicted in Figure 6.

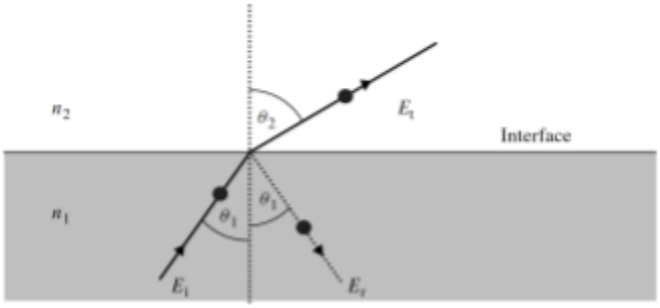

Figure 6: Transmittance and reflectance at the incidence of electric field on the interface of two media; • means out of the paper plane

Similarly in the *Transverse Magnetic* (TM) condition, the magnetic field vector is perpendicular to the incidence plane. Based on trigonometric operations on electric field lines in Figure 6, Frensel formulae define reflection coefficients in both TE and TM modes are defined as follows:

$$r_{\mathrm{TE}} = \frac{n_1 \cos\theta_1 - n_2 \cos\theta_2}{n_1 \cos\theta_1 + n_2 \cos\theta_2} \qquad (10)$$

$$r_{\mathrm{TM}} = \frac{n_2 \cos\theta_1 - n_1 \cos\theta_2}{n_2 \cos\theta_1 + n_1 \cos\theta_2} \qquad (11)$$

With the aid of Snell's law (Equation 6), Equation 10, 11 could be re-written as:

$$r_{\mathrm{TE}} = \frac{n_1 \cos\theta_1 - \sqrt{n_2^2 - n_1^2 \sin^2\theta}}{n_1 \cos\theta_1 + \sqrt{n_2^2 - n_1^2 \sin^2\theta}} \qquad (12)$$

$$r_{\mathrm{TM}} = \frac{n_2^2 \cos\theta_1 - n_1\sqrt{n_2^2 - n_1^2 \sin}}{n_2^2 \cos\theta_1 + n_1\sqrt{n_2^2 - n_1^2 \sin}} \qquad (13)$$

In case the incidence angle is less than the critical angle, solely partial reflection is exhibited and the reflection coefficient is real. On the other hand, when the angle of incidence is larger than the critical angle, TIR occurs the whole light wave is reflected, meaning that |*r*| equals one. As seen in Equation 10. the terms inside square roots become negative in this case, meaning that *r* is a complex number, imposing a phase shift on the reflected wave. Thus, r could be defined as:

$$r = e^{j\phi} \qquad (14)$$

where phase shifts in TE (ϕ_{TE}) and TM (ϕ_{TM}) are calculated by:

$$\phi_{\mathrm{TE}} = 2\tan^{-1}\frac{\sqrt{\sin^2\theta_1 - \left(\frac{n_2}{n_1}\right)^2}}{\cos\theta_1} \qquad (15)$$

$$\phi_{\mathrm{TM}} = 2\tan^{-1}\frac{\sqrt{(\frac{n_1}{n_2})^2 \sin^2\theta_1 - 1}}{(\frac{n_2}{n_1})\cos\theta_1} \qquad (16)$$

To quantify the magnitude of 'partially' transmitted and reflected waves, electromagnetic waves are described in terms of power their power that is reflected or transmitted, and that power is described by *Poynting vector*, symbolized by S (in W/m^2). Being the vector product of electric and magnetic vectors, the Poynting vectors designate the direction and magnitude of the power flow of the wave; S is determined by:

$$S = \frac{1}{Z}E^2 = \sqrt{\frac{\varepsilon_m}{\mu_m}}E^2 \qquad (17)$$

for E is the electric field vector, μ_m is permeability of the medium, ε_m is the permittivity of the medium, and Z is the impedance of the medium. Thus, *reflectance* (R) could be defined as the ratio between the Poynting vector of reflected and incident wave:

$$R = \frac{S_r}{S_i} = \frac{\frac{1}{Z}E_r^2}{\frac{1}{Z}E_i^2} = r^2 \qquad (18)$$

3.3. Modes of Planar Waveguide

To characterize the wave propagation in the waveguide, a planar waveguide (simplest waveguide) depicted in Figure 7 is considered. In the planar waveguide, light is confined in the x direction by TIR, propagating in the direction of wavenumber (k), which is also related to wavenumber in free space (k_0) by n of medium:

$$k = k_0 n \qquad (19)$$

Since the wave number (k) has two components (κ in x direction and β in z direction), it could be decomposed as:

$$\beta = n_1 k_0 \sin\theta_1 \qquad (20)$$

$$\kappa = n_1 k_0 \cos\theta_1 \qquad (21)$$

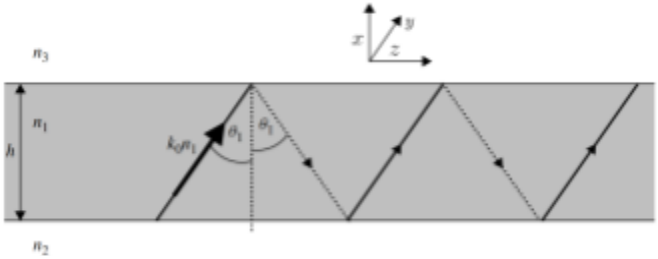

Figure 7: propagation of light ray in planar waveguide

It has been established before that a phase shift is associated with TIR and the phase shift was defined as the product of propagation constant and distance in Equation 5. Thus, by assuming an ideal TIR, all the phase shifts imposed on the propagating wave in one complete cycle in x direction back and forth of distance of $2h$, could be determined by:

$$\phi_h = 2\kappa h = 2k_0 n_1 h\cos\theta_1 \qquad (22)$$

Nonetheless, it is only desired to obtain the total phase change imposed in one complete cycle, but as in Equation 13 phase changes are also introduced at the reflection at lower and upper waveguide interfaces. Accordingly, upper and lower phase shifts could be subtracted from the expression to isolate the phase change in one cycle. However, for the wave through the waveguide to be preserved, the summation of phase shift is to be an integer multiple (m) of 2π, modifying Equation 18 into:

$$2k_0 n_1 h\cos\theta_1 - \phi_u - \phi_l = 2m\pi \qquad (23)$$

Since m is an integer, there exist only discrete solutions, or angles (θ_1), for Equation 19 to be solved. Therefore, it is not sufficient to say that the only condition for TIR to occur is to exceed the critical angle as suggested in section 2.2. Intuitively, a corresponding propagation constant (k) in y and z direction will exist for each discrete solution. By convention, each solution is called a *mode of propagation*, in which the value of m specifies the mode number. Modes are written as a combination of polarisation and mode number, for instance, the *fundamental mode* is written as TE_0, where TE indicates polarisation and the number zero indicates value of m.

The waveguide depicted in Figure 7 is a symmetrical waveguide since the upper and lower cladding has the same refractive index value; thus, $\phi_u = \phi_l$ and by using Equation 15 a in TE mode, the equation could be modified into:

$$2k_0 n_1 h \cos\theta_1 - 4\tan^{-1}\left[\frac{\sqrt{\sin^2\theta_1 - (n_2/n_1)^2}}{\cos\theta_1}\right] = 2m\pi \quad (26)$$

Isolating the mode number and propagation constant on one side of the equation yields:

$$\tan\left[\frac{k_0 n_1 h\cos\theta_1 - m\pi}{2}\right] = \left[\frac{\sqrt{\sin^2\theta_1 - (n_2/n_1)^2}}{\cos\theta_1}\right] \quad (27)$$

Correspondingly, in the case of TM polarization, Equation 15 could be used. However, from Equation 7, it is visible that θ_1 equals $\frac{n_2}{n_1}$. Thus, approximately, the right side of Equation 25 reduces to zero. Additionally, because the value of θ_1 decreases as the mode number increases, at $\theta_1 = \theta_c$, which is the lowest value possible for θ_1, the equation becomes:

$$\frac{k_0 n_1 h\cos\theta_c - m_{max}\pi}{2} = 0 \quad (26)$$

By resorting the equation for m_{max}, the max mode number (including 0) is:

$$m_{max} = \frac{k_0 n_1 h\cos\theta_c}{\pi} \quad (27)$$

3.4. Modes of Planar Waveguide

To validate the assumptions related to electric and magnetic waves made in the above sections, it would be appropriate to address Maxwell's equations in a dielectric medium, relating electric field (E) and magnetic field (H) [10]:

$$\nabla \times \tilde{E} = -\mu_0 \frac{\partial \tilde{\mathrm{H}}}{\partial t} \quad (28)$$

$$\nabla \times \tilde{H} = \varepsilon_0 n^2 \frac{\partial \tilde{\mathrm{E}}}{\partial t} \quad (29)$$

where μ_0 is the permeability of vacuum and ε_0 is the permittivity of vacuum. And ∇ is the Del operator, given by:

$$\nabla = \frac{\partial}{\partial x} i + \frac{\partial}{\partial y} j + \frac{\partial}{\partial z} k \quad (30)$$

In this context, it would be beneficial to renew the definition of wavenumber in a vacuum as:

$$k = \omega\sqrt{\varepsilon_0\mu_0} = \frac{\omega}{c} \quad (31)$$

for c is the velocity of light in a vacuum. Since a planar waveguide is being analyzed, plane propagation of electromagnetic waves is given by:

$$\tilde{E} = E(x,y)\exp\left[j(\omega t - \beta z)\right] \quad (32)$$

$$\tilde{H} = H(x,y)\exp\left[j(\omega t - \beta z)\right] \quad (33)$$

Equations 32, 33 could be substituted in Equations 28, 29, the following set of equations for each electric and magnetic field could be obtained:

$$\begin{aligned}\frac{\partial E_z}{\partial y}+j\beta E_y&=-j\omega\mu_0 H_x\\ -j\beta E_x-\frac{\partial E_z}{\partial x}&=-j\omega\mu_0 H_y\\ \frac{\partial E_y}{\partial x}-\frac{\partial E_x}{\partial y}&=-j\omega\mu_0 H_z\end{aligned}\tag{34}$$

$$\begin{aligned}\frac{\partial H_z}{\partial y}+j\beta H_y&=j\omega\varepsilon_0 n^2 E_x\\ -j\beta H_x-\frac{\partial H_z}{\partial x}&=j\omega\varepsilon_0 n^2 E_y\\ \frac{\partial H_y}{\partial x}-\frac{\partial H_x}{\partial y}&=j\omega\varepsilon_0 n^2 E_z.\end{aligned}\tag{35}$$

Considering the slab waveguide shown in Figure 7, the electromagnetic waves are not confined in y direction (only confined in x direction). Thus, both the electric (E) and magnetic (H) fields do not vary with distance in y direction, or mathematically:

$$\begin{aligned}\frac{\partial E}{\partial y}&=0\\ \frac{\partial H}{\partial y}&=0\end{aligned}\tag{36}$$

by substituting Equation 36 into both Equations 34 andEquations 35, the two independent electromagnetic modes (TE and TM) are acquired, where the TE mode satisfies this wave equation:

$$\frac{d^2E_y}{dx^2}+(k^2n^2-\beta^2)E_y=0\tag{37}$$

for

$$\begin{aligned}H_x&=-\frac{\beta}{\omega\mu_0}E_y\\ H_z&=\frac{j}{\omega\mu_0}\frac{dE_y}{dx}\\ E_x=E_z&=H_y=0\end{aligned}\tag{38}$$

Since $E_z=0$, the electric field exists in the perpendicular to the z-axis, hence the polarisation is TE. Alternatively, the TM mode satisfies this wave equation:

$$\begin{aligned}&\frac{d}{dx}\left(\frac{1}{n^2}\frac{dH_y}{dx}\right)+\\ &\left(k^2n^2-\frac{\beta^2}{n^2}\right)H_y=0\end{aligned}\tag{39}$$

for

$$\begin{aligned}e_x&=\frac{\beta}{\omega\varepsilon_0 n^2}h_y\\ e_z&=-\frac{j}{\omega\varepsilon_0 n^2}\frac{dh_y}{dx})\\ e_y=h_x&=h_z=0\end{aligned}\tag{40}$$

Correspondingly to the TE mode, $H_z=0$. Thus, the magnetic field is perpendicular to the z-axis, hence, it is TM mode.

To calculate the propagation constants (k and β), electric field E, and magnetic field H for TE and TM can be acquired by solving Equations 37, 39 utilizing eigenvalue equations, which is explained in depth in [9]. After solving the eigenvalue equations, the propagation constants will be obtained along with the eigenvalue of the waveguide (modes in TE and TM modes). However, it is worth explaining the *effective refractive index* for its fundamental importance in this study and in Maxwell's equations-based analysis in general. Generally, the

refractive index in a medium could be, with the aid of Equation 3, defined as:

$$n = \frac{c}{v} = \frac{\lambda_0 \nu}{\lambda \nu} = \frac{\lambda_0}{\lambda} = \frac{k}{k_0} \qquad (41)$$

where v is the frequency in all media and λ_0, is the wavelength in vacuum. Thus, an effective index is merely a ratio of the velocity, wavenumber, or wavelength of light in a vacuum to light in another medium. However, in the realm of waveguides, light has different propagation velocities for each mode in a given polarization. Thus, the effective refractive index is used to denote the ratio between the velocity of light in a vacuum to its velocity in a given polarisation mode whilst the propagation in z direction is as follows:

$$n_{eff} = \frac{c}{v_z} = \frac{\lambda_0 \nu}{\lambda_z \nu} = \frac{\lambda_0}{\lambda_z} = \frac{\beta}{k_0} \qquad (42)$$

Also, as modes only exist in the case of TIR and effective index is the quotient of propagation constant and free space number, the value of n_{eff} will be higher than that of lower and upper cladding albeit lower than guiding layers (middle layer) as depicted in Figure 7 refractive index.

Finally, as it has been mentioned in section 3.2, the wave is quantified in terms of the Poynting vector or power carried by the wave, which is to be defined in terms of electric (E) and (H) as:

$$P = \int_0^1 dy \int_{-\infty}^{\infty} \frac{1}{2}(E \times H^*) \cdot \mathrm{u}_z dx \int_{-\infty}^{\infty} \frac{1}{2}\left(E_x H_y^* - E_y H_x^*\right) \qquad (43)$$

where * denotes a complex conjugate. The equation could be rewritten for TE mode with the aid of Equation 37 as:

$$P = \frac{\beta}{2\omega\mu_0} \int_{-\infty}^{\infty} |E_y|^2 dx \qquad (44)$$

And correspondingly, in the case of TM polarisation, the Poynting vector could be, with the aid of Equation 29 written as:

$$P = \frac{\beta}{2\omega\varepsilon_0} \int_{-\infty}^{\infty} \frac{1}{n^2} |H_y|^2 dx \qquad (45)$$

Numerical computational methods incorporated for solving the above electromagnetic wave equations and visualization of power flow are to be explained in the following sections related to the modeling and simulation of the device.

3. Waveguide Birefringence

As illustrated in section 3.2, the fundamental mode ($m = 0$) has two orthogonally polarized components. In the case of symmetric waveguides (for example, planar waveguides), the propagation constants in both TE and TM modes are equal in value due to identical geometrical boundary parameters [8]. However, due to imperfect manufacturing conditions (fabrication errors, stress, or fluctuations in temperature), waveguides, even if designed to be symmetric, are not perfectly symmetric [8]. Also, by extension, the effective indices (n_{eff}) of TE and TM modes are affected and different in the two modes. The aforesaid difference in value in the effective refractive indices in the two modes is known as

birefringence (Δn_{eff}). Mathematically, birefringence is given by:

$$\Delta n_{eff} = n_{eff}^{\mathrm{TM}} - n_{eff}^{\mathrm{TE}} \tag{46}$$

where n_{eff}^{TM} is the effective refractive index in TM mode and n_{eff}^{TE} is the effective refractive index in TE mode. Additionally, waveguide birefringence (Δn_{eff}) is the summation of stress-induced birefringence (Δn_{stress}) and geometrical birefringence (Δn_{geo}):

$$\Delta n_{eff} = \Delta n_{geo} + \Delta n_{stress} \tag{47}$$

It should be noted that geometrical birefringence is caused by the waveguide asymmetry [9], whereas stress-induced birefringence is caused by anisotropic stress in the waveguide [11].

Birefringence is considered a concerning issue in integrated optical systems as it causes polarisation-dependant modulation (PDM) in electro-optic modulators (devices allowing control of amplitude, phase, and polarization of light waves) [12]. In addition, in the field of sensors and coherent communication systems, polarisation-dependent sensitivity (PDS) is caused by birefringence [13]. Not to forget that all of the aforementioned devices incorporate waveguides as integral components in their design. Further, a high birefringence implies a significant difference between propagation speeds of two-bit streams in the two modes [6]. Birefringence is also a metric describing the impact of geometry/ material properties on mode (quantified in terms of power) [6]. Thus, Δn_{eff} has an effect on optical power flow. It is clear that birefringence control is essential for the non-faulty operation of a variety of optical devices.

For the management of polarization, two methodologies have been proposed. One is to utilize polarization splitter devices to separate the TE and TM to avoid birefringence problems and the other is to engineer devices to be independent of polarization [14]. It was shown in [15], that principally, a birefringence-free waveguide with a relatively large cross-section can be attained by geometrical optimization of the core. However, according to [16], such methodology for birefringence elimination is not feasible for waveguides of smaller dimensions like the one considered in this study (buried-core square waveguide). Taking into account that the waveguide's core geometry is crucial for determining device performance, making it less attractive to modify it to not negatively affect the performance of the device. Additionally, the fabrication of waveguides with a low tolerance in terms of dimensional errors makes this approach more challenging for the current fabrication technologies [7]. For such limitations, a widely used approach for birefringence control, stress engineering, has been suggested by adjusting fabrication conditions alongside properties of waveguide's material to control the photoelastic effect, and hence birefringence. Next, the photoelastic effect is to be described and, afterwards, its impacts on device performance.

5. Photoelastic Effect

Photoelastic effect is a phenomenon causing the stress-induced change in refractive indices [17] in optical waveguides. Since waveguides are dielectric media, it would be advantageous to revisit a fundamental parameter, permittivity (ε). Permittivity determines the material's ability to be polarised under an applied field [9]. Another essential parameter is the dielectric constant (κ), which relates a dielectric's permittivity to that of a vacuum:

$$\kappa = \frac{\varepsilon}{\varepsilon_0} \tag{48}$$

The dielectric constant is also related to the material's refractive index:

$$\kappa = n^2 \tag{49}$$

When considering a cubic anisotropic (having dissimilar refractive indices along different

crystallographic axes) dielectric material, the dielectric constant takes tensor form as:

$$\kappa = \begin{pmatrix} n_{xx}^2 & n_{xy}^2 & n_{xz}^2 \\ n_{xy}^2 & n_{yy}^2 & n_{yz}^2 \\ n_{xz}^2 & n_{yz}^2 & n_{zz}^2 \end{pmatrix} \tag{50}$$

where $n_{xx}, n_{yy}, n_{zz}, n_{xy}, n_{xz}$, and n_{yz} are the refractive indices along crystallographic axes. According to the photoelastic effect, refractive indices are changed by stress and strain applied to the media. In the case of cubic structure, the refractive index, and accordingly the dielectric tensor, and strain (γ) are related by the follows [18]:

$$\Delta \begin{pmatrix} \frac{1}{n_{xx}^2} \\ \frac{1}{n_{yy}^2} \\ \frac{1}{n_{zz}^2} \\ \frac{1}{n_{yz}^2} \\ \frac{1}{n_{xz}^2} \\ \frac{1}{n_{xy}^2} \end{pmatrix} = \begin{pmatrix} p_{11} & p_{12} & p_{12} & 0 & 0 & 0 \\ p_{12} & p_{11} & p_{12} & 0 & 0 & 0 \\ p_{12} & p_{12} & p_{11} & 0 & 0 & 0 \\ 0 & 0 & 0 & p_{44} & 0 & 0 \\ 0 & 0 & 0 & 0 & p_{44} & 0 \\ 0 & 0 & 0 & 0 & 0 & p_{44} \end{pmatrix} \times \begin{pmatrix} \gamma_{xx} \\ \gamma_{yy} \\ \gamma_{zz} \\ \gamma_{yz} \\ \gamma_{xz} \\ \gamma_{xy} \end{pmatrix} \tag{51}$$

for p_{11}, p_{12}, and p_{44} are strain-optic constants. Further, refractive indices, utilizing stress-strain relations, are related to stress by the following equation [18]:

$$\begin{pmatrix} n_{xx} \\ n_{yy} \\ n_{zz} \\ n_{yz} \\ n_{xz} \\ n_{xy} \end{pmatrix} = \begin{pmatrix} n_0 \\ n_0 \\ n_0 \\ 0 \\ 0 \\ 0 \end{pmatrix} - \begin{pmatrix} C_1 & C_2 & C_2 & 0 & 0 & 0 \\ C_2 & C_1 & C_2 & 0 & 0 & 0 \\ C_2 & C_2 & C_1 & 0 & 0 & 0 \\ 0 & 0 & 0 & C_3 & 0 & 0 \\ 0 & 0 & 0 & 0 & C_3 & 0 \\ 0 & 0 & 0 & 0 & 0 & C_3 \end{pmatrix} \times \begin{pmatrix} \sigma_{xx} \\ \sigma_{yy} \\ \sigma_{zz} \\ \sigma_{yz} \\ \sigma_{xz} \\ \sigma_{xy} \end{pmatrix} \tag{52}$$

for that photoelastic coefficients C_1, C_2, and C_3, which are related to strain-optic constants as [18]:

$$\begin{aligned} C_1 &= \frac{n_0^3(p_{11} - 2vp_{12})}{2E} \\ C_2 &= \frac{n_0^3[p_{12} - v(p_{11} - p_{12})]}{2E} \\ C_3 &= \frac{n_0^3\, p_{44}}{2G} \end{aligned} \tag{53}$$

where E is the Young's modulus, G is shear modulus, and ν is Poisson ratio. Nonetheless, because we are tackling birefringence, the main concern is the change of refractive indices in the three main axes. Thus, Equation 52 could be written in linear form n_x, n_y, and n_z [9]:

$$\begin{aligned} n_x &= n_{x0} - C_1\sigma_x - C_2[\sigma_y + \sigma_z] \\ n_y &= n_{y0} - C_1\sigma_y - C_2[\sigma_z + \sigma_x] \\ n_z &= n_{z0} - C_1\sigma_z - C_2[\sigma_x + \sigma_y] \end{aligned} \tag{54}$$

Therefore, for the photoelastic effect to be quantified, the three primary stresses, caused by thermal mismatching, along the x, y, and z axes are to be determined, which is done by utilizing the plane strain approximation alongside numerical techniques. Noting that after the change in refractive indices matrix is obtained, it is used as material data for the simulation software for determining change in

refractive indices, birefringence, and, subsequently, waveguide's optical power flow.

6. Device Modelling and Simulation

6.1. Device Overview

Before demonstrating the simulation steps and numerical techniques implemented, a brief description of the device is to be established. Regarding device fabrication, high-temperature thermal annealing is integral for buried-core square waveguide depicted in Figure 8. Firstly the underlying layer of the silicon film (wafer) is deposited via flame hydrolysis deposition (FHD) or chemical vapor deposition (CVD) [2]. Secondly, the silica under cladding is typically structured by steam oxidation at high temperatures. Thirdly, lithography is implemented to define the geometry of the square core on the buffer, whereas under cladding is etched for forming the core layer [6]. Fourthly, the upper cladding is non-consecutively deposited with intermediate annealing, then final annealing. Ultimately, to increase wave confinement, the core is doped with phosphorus to raise the refractive index, while the upper cladding is boron-doped to reduce the refractive index [6]. Such structure, formed at high temperatures, manifests both intrinsic stress (due to defect-inducing fabrication) and thermal stress (due to different thermal expansion coefficients of each layer). However, in this simulation, the intrinsic stress will be neglected as its value is relatively insignificant [19]. Among all of the annealing temperatures, the one to be considered is the final annealing temperature (at 1000 °C), where the device operation temperature is 20°C. Thus the T for the calculation of thermal stresses is 980 K.

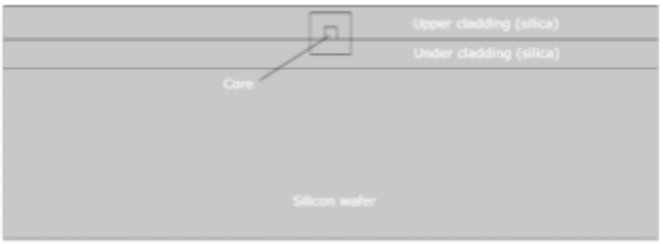

Figure 8: buried-core square waveguide geometry with corresponding materials

6.2. Definitions and Geometry

As depicted in Figure 9, the first step in the simulation is to define global variables to be used by the software. Both the optical and mechanical material parameters for silicon and silica used in the simulation are exhibited in Table 1, where n is the refractive index measured in wavelength of 1.55 (operational wavelength of the device) μm, α is thermal expansion coefficient, E is Young's modulus, ν is Poisson's ratio, and C_1 and C_2 are first and second-degree photoelastic coefficients, respectively. The reason that only the photoelastic coefficients of silica are mentioned is that even though the stress will be evaluated for the whole structure, the photoelastic effect will be computed only for the core, where the optical power is confined.

Regarding the second stem, geometry creation, as shown in Figure 8, the silicon wafer has dimensions $320 \times 83\ \mu m$, which acts as a base for the photonic circuit components. The upper two layers have the same width as the substrate, but the lower cladding has a thickness of $14\ \mu m$ and the upper cladding's thickness is $16\ \mu m$. The core, responsible for wave confinement, has square dimensions with side length $6 \mu m$, where the square around the core is added to merely enclose the computational domain for stress and mode analysis. The dimensions of the core are optimized to ensure mode confinement and that no power is lost. However, the width of the structure is rather arbitrary as long it is sufficiently greater than the height of the structure.

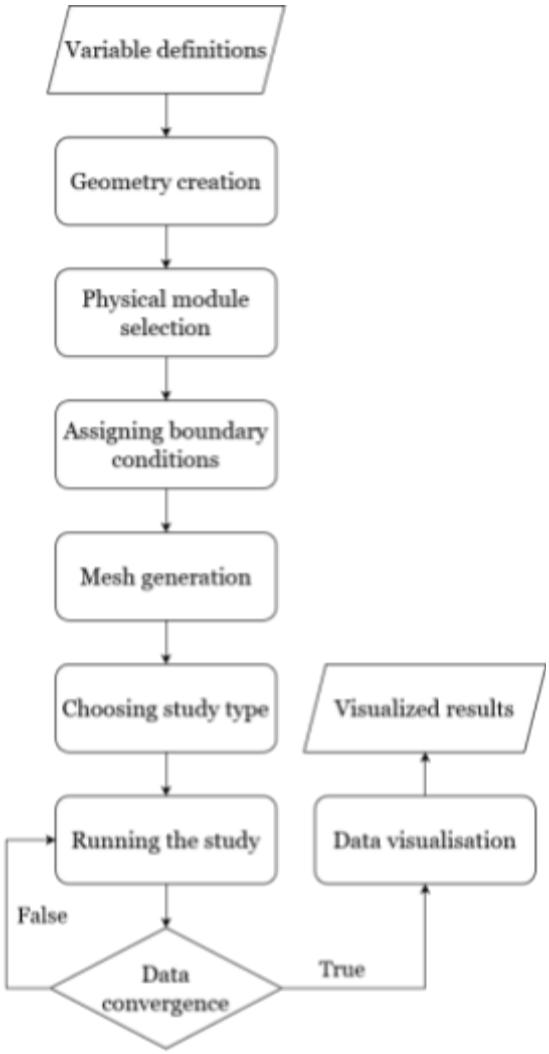

Figure 9: simulation steps in COMSOL

Material	Parameter	Value
Silicon (Si)	n	3.5
	α (10^{-6} K^{-1})	2.5
	E (GPa)	110
	ν	0.19
Silica (SiO_2)	n	1.445
	α (10^{-6} K^{-1})	0.35
	E (GPa)	78
	ν	0.17
General	C_1 (10^{-12} m^2/N)	0.6
	C_2 (10^{-12} m^2/N)	4.2

Table 1: Optical and mechanical properties of Si (substrate) and SiO_2 (core and upper cladding), obtained from [9] and modified from COMSOL material library

6.3 Stress Analysis

The third step in Figure 9, is the choice of physical modules, which are software packages containing the physical definitions and laws to specify the type of simulation being done. First, the *Solid Mechanics* module is chosen, and following it are boundary definition and mesh generation. However, before delving into the steps related to setting up the module, the numerical method utilized by the software ought to be clear.

As seen in the previous sections, the majority of equations defining laws of physics are in the form of Partial Differential Equations (PDEs). Such PDEs describing increasingly complex systems can not be solved with analytical methods. Instead, a range of numerical techniques has been developed to approximate these equations, typically, via discretizations (body is broken into discrete elements as illustrated in Figure 10), approximating PDEs to numerical model equations to be solved via numerical methods. Among these techniques used to approximate PDEs is the Finite Element Method (FEM), which was initially developed for the stiffness analysis of airplanes [20]. Thus, it was designed for stress analysis, making it the most typical application of FEM. To explain the FEM approach for stress analysis in the waveguide, the mathematical model describing the system is to be illustrated, starting with the *energy principle*.

It is a well-established theory that when a body is subjected to thermal stress, chemical bonds tend to lengthen, changing the total potential energy of the system by a value equal to external work applied (V) as the strain energy (U) is getting released (lessened), reducing potential energy (Π) to its minimum. Such principle is known as the energy principle [21], where the total potential energy is given by:

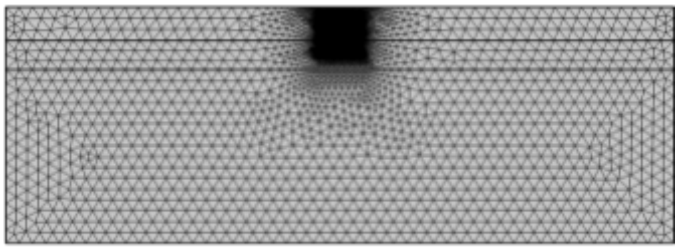

Figure 10: mesh elements of waveguide

For a body that is long along the z-axis relative to its cross-section (e.g., the waveguide considered in this study), the out-of-plane strain (ε_z) is assumed to be zero (excluding both ends of the structure), meaning that [9]:

$$\varepsilon_z = 0 \tag{55}$$

Based on that assumption, the stress analysis is deemed as a *plane strain problem*, in which the relation between displacement and strain is [22]:

$$\begin{aligned} \varepsilon_x &= \frac{\partial u}{\partial x} \\ \varepsilon_y &= \frac{\partial v}{\partial y} \end{aligned} \tag{56}$$

Strain is also related to stress as follows:

$$\begin{aligned} \varepsilon_x &= \frac{1}{E}[\sigma_x - \nu(\sigma_y + \sigma_z)] + \alpha\Delta T \\ \varepsilon_y &= \frac{1}{E}[\sigma_y - \nu(\sigma_z + \sigma_x)] + \alpha\Delta T \\ \varepsilon_z &= \frac{1}{E}[\sigma_z - \nu(\sigma_x + \sigma_y)] + \alpha\Delta T \end{aligned} \tag{57}$$

where ΔT is, in the case of this device, the difference between reference temperature at thermal annealing and operational temperature ($\Delta T = 980K$). Equation 55 could be substituted in Equation 57 to be rewritten to define each one of the three principle stresses as a function of strain as follows [9]:

$$\begin{aligned} \sigma_x &= \frac{E}{(1+\nu)(1-2\nu)}[(1-\nu)\varepsilon_x + \nu\varepsilon_y] \\ &\quad - \frac{\alpha E\Delta T}{(1-2\nu)} \\ \sigma_y &= \frac{E}{(1+\nu)(1-2\nu)}[(1-\nu)\varepsilon_y + \nu\varepsilon_x] \\ &\quad - \frac{\alpha E\Delta T}{(1-2\nu)} \\ \sigma_z &= (\sigma_x + \sigma_y)\nu - \alpha E\Delta T \end{aligned} \tag{58}$$

From the above equations, it is shown that the three main stresses could be evaluated using FEM as functions of strain, which is in turn a function of displacement. Further, for quantifying the equivalent stress of each element in the mesh alongside visualization, von Mises equivalent stress (σ_{VM}), depicted in Figure 57, for each element could be evaluated as a function of three principle stresses as follows:

$$\sigma_{VM} = \frac{1}{\sqrt{2}}\sqrt{(\sigma_x - \sigma_y)^2 + (\sigma_y - \sigma_z)^2 + (\sigma_z - \sigma_x)^2} \tag{59}$$

As shown in Figure 11, the waveguide structure is deformed due to thermally-induced stresses. However, the equivalent stress varies only slightly horizontally. On the other hand, vertically, the strains are more significant, meaning that the majority of changes in optical properties will result from vertical stresses. The change in refractive indices due to the photoelastic effect is described with Equation 54, producing the matrix of new refractive indices along principle axes to be used to define variables in the mode analysis to determine the effects of stresses on waveguide birefringence. The numerical procedures for the mode analysis will be subsequently briefly described.

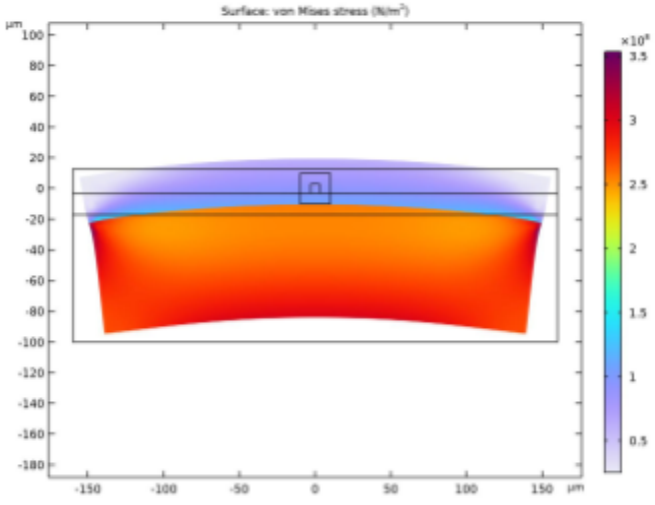

Figure 11: von Mises stress distribution on waveguide structure

6.4 Mode Analysis

After finishing choosing and defining the first physics module shown in Figure 9, the second physics module chosen is *Electromagnetic waves*, which similarly relies on FEM to approximate solutions of PDEs derived from basic physics equations, wave equations, rather than stress-strain relation. For clarity, the boundary conditions are the same as geometrical boundaries, where for the electromagnetic waves it is the square computational domain around the waveguide's core, but for the previous module, solid mechanics, the boundary conditions are the geometric boundaries of the whole structure. For continuity, the mesh on which the FEM is carried on is depicted in Figure 10.

The assumptions, on which the FEM is based, start with defining the electric field as in Equation 32. However, the equation could be further simplified into [9]:

$$\nabla^2 E + \left[k^2 n^2(x,y) - \beta^2\right] E(x,y) = 0 \quad (60)$$

Then, FEM converts Equation 60 into a variational problem with the apt boundary conditions, where the solution of wave equation could be acquired via solving for $$E$$ that satisfies the stationary condition of the following functional (a function that of vector domain and a scalar range) [9]:

$$\Psi[E] = \frac{1}{2}\int_{-\infty}^{\infty}\int_{-\infty}^{\infty}\left[\left(\frac{\partial E}{\partial x}\right)^2 + \left(\frac{\partial E}{\partial y}\right) - (k^2 n^2 - \beta^2)E^2\right]dxdy \quad (61)$$

Next, the mesh is generated, where the structure is divided into $$N$$ discrete triangular elements as depicted in Figure 10 ($$N = 34700$$) and electric field as a function of $$x$$ and $$y$$ coordinates in each element denoted by $$i$$ could be approximately given by the following linear function [9]:

$$E(x,y)^i = a_0^i + a_1^i x + a_2^i y \quad (62)$$

where $$a_0^i$$, $$a_1^i$$, and $$a_2^i$$. It should be noted that for the elements to be in triangular form (formed of 3 points each), each node has the same linear function of Equation 62. Thus, Equation 62 is substituted in Equation 61 for each element and the solution over the entire domain for the electric field distribution for each mode and propagation constant is given as the summation of all the individual elements:

$$\Psi = \sum_{i=1}^{N} \Psi^i \quad (63)$$

Further, the effective index ($$n_{eff}$$) for TE and TM mode is given by Equation 42. Since the accuracy of the solution extracted is directly dependent on the number of elements (mesh density), a convergence analysis was performed as shown in Figure 9 after running the study to find the optimal number of mesh elements. Notice that the density of elements in the computational domain around the waveguides' core in Figure 10, is relatively higher because the electric field is confined and frequently changing in this area. Hence, the photoelastic effect is only determined for this area.

Lastly, data visualization is performed. For instance, as shown in Figure 12 the optical power density distribution is visualized, where red means higher intensity and blue means lower intensity

($$\mathrm{W/m^2}$$). It could be observed that in the higher number modes ($$\mathrm{TE}_1$$ and $$\mathrm{TM}_14$) in Figure 12 have significant portions of optical energy are dispersed into the upper and lower cladding, rendering higher modes more sensitive to core's geometry and boundary conditions. Thus, they have more significant changes when compared to fundamental modes due to the photoelastic effect as it is explained in the following section alongside other parameters of the waveguide.

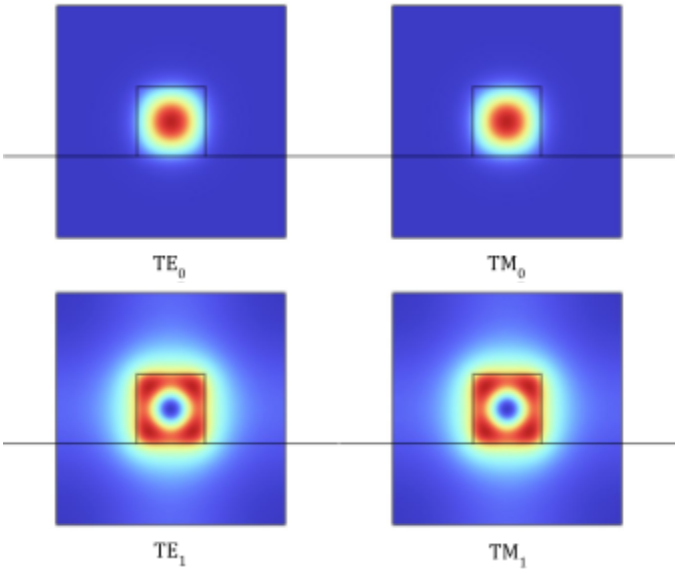

Figure 12: power density (W/m^2) distribution of first four fundamental modes without photoelastic effect

7. Results

7.1. Effective Refractive Indices

After the software evaluated the propagation constant ($$\beta$$) and wavenumber ($$k$$) from Equation 60, the refractive indices for the first four modes were evaluated using Equation 42, where their respective values are shown in Figure 13. From the figure, the shift is significant, causing a change in birefringence, defined in Equation 46.

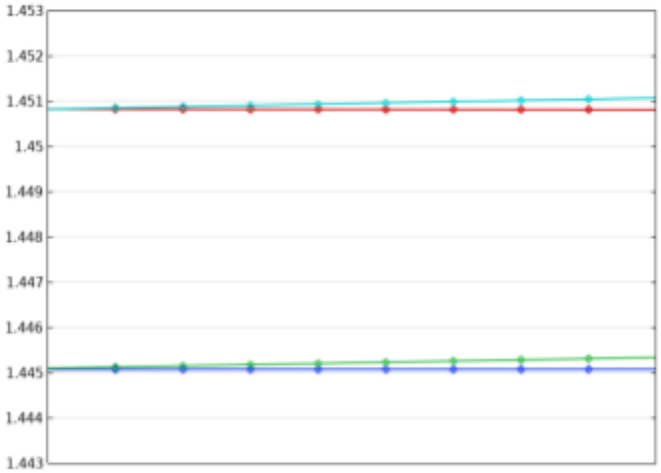

Figure 13: Effective refractive indices for the first four modes without (left) and with (right) photoelastic effect

7.2. Birefringence

Due to the change in refractive indices in TE and TM modes, birefringence is changed as shown in Figure 13. However, it could be shown that, due to the nature of equivalent stress distribution in Figure 11, birefringence is approximately constant throughout the horizontal axis, but varies substantially along the vertical axis. Inferred from this observation, thermal stresses during the fabrication process have an insignificant impact on the side edges of the waveguide's core, rendering geometrical optimization of the geometry ineffective as mentioned before in section 4.

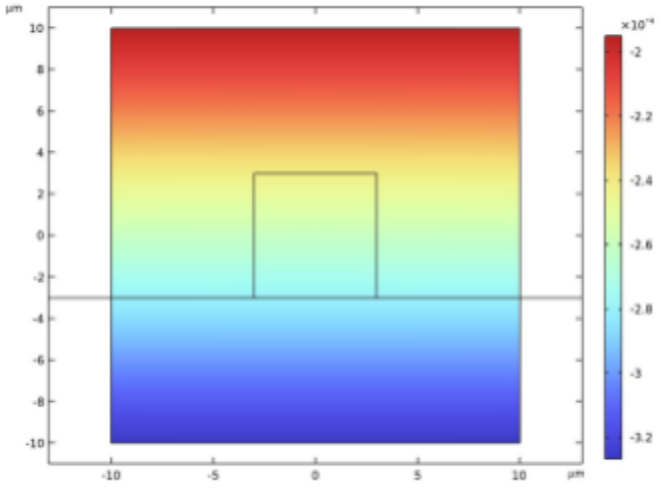

Figure 14: birefringence value gradient on waveguide cross section

7.3. Power Flow

Due to birefringence in the waveguide's core, power density distribution has been affected as shown in Figure 15. The change is more evident in higher modes manifested in Figure 15 (TE_1) and (TM_1), where a mode split has occurred. Additionally, the optical power was more confined in TE_1 and TM_1 under the photoelastic effect, which is advantageous for low-loss waveguide applications. It could be inferred that both birefringence and optical power density distribution are heavily affected by anisotropic stress and its configuration. Thus, instead of geometrical optimization of the waveguide's geometry, which is impractical and ineffective for micron-size waveguides, optimization of mechanical material properties of the cladding layers can potentially control device performance. Additionally, the optimization of fabrication conditions (mainly temperature) can be used to control the thermally-induced anisotropic stresses in the waveguide structure and to avoid undesired effects.

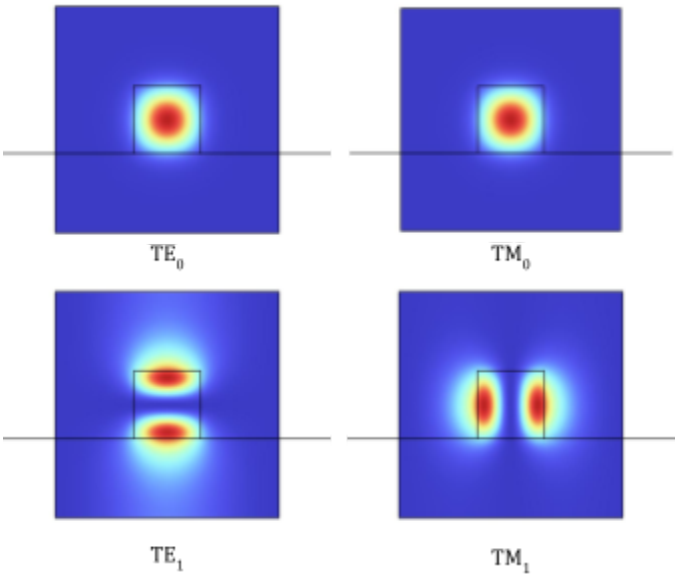

Figure 16: power density (W/m^2) distribution of first four fundamental modes with photoelastic effect

8. Conclusion

This paper aimed to understand and visualize the photoelastic effect and its impacts on a buried-core square silicon waveguide due to thermally-induced stresses resulting from high-temperature manufacturing processes. A simulation was performed in COMSOL Multiphysics for this sake, utilizing the FEM for doing numerical calculations. Further, simulation steps and underlying principles of the software were described, with a focus on FEM. It was possible to determine the equivalent stress distribution in the waveguide, exploiting the plane strain assumption. From the distribution, it was visible that stress was significantly varying along the vertical axis while being approximately constant along the horizontal axis. Subsequently, the effect of stress on effective refractive indices, birefringence, and optical power distribution were determined. It was also found that the effect of anisotropic thermally-induced stresses was more substantial on higher modes, where mode splits occurred. It was also evident that by optimizing mechanical properties of the cladding and/or manufacturing conditions birefringence, subsequent performance-governing parameters could be controlled. For brevity, the research investigated the photoelastic effect on a silicon waveguide and its impact on performance-governing parameters, deducing that optimizing mechanical properties and manufacturing conditions could control birefringence. Nonetheless, it is recommended that future researchers leverage other approaches and modifications to this model, which could potentially be using the generalized plane-strain assumption instead of the ordinary one used in this study. In addition, stress engineering could also be a potentially effective other material platform of waveguides exhibiting the significant photoelastic effect (e.g., alternative III-V semiconductor waveguides).

9. Acknowledgement

We would like to extend our deepest gratitude to the African Research Program for Leaders (ARPL) for shaping our intellectual curiosity and guiding us in our academic journey. We are also thankful to the African Leadership Academy (ALA) for creating an environment that empowers young leaders across the continent.

10. References

[1] H. Barlow, "Optical fibre transmission in the TE01 mode," *Journal of Physics D: Applied Physics*, vol. 13,

no. 3, pp. 369--375, 1980, doi: 10.1088/0022-3727/13/3/007.

[2] T. Reed and P. Knights, *Silicon Photonics: An Introduction*. Electronically published: Wiley, 2004.

[3] H. Sattari *et al.*, "Silicon photonic microelectromechanical systems add-drop ring resonator in a foundry process," *Journal of Optical Microsystems*, vol. 2, no. 04, 2022, doi: 10.1117/1.jom.2.4.044001.

[4] R. Soref and B. Bennett, "Electrooptical effects in Silicon," *IEEE Journal of Quantum Electronics*, vol. 23, no. 1, pp. 123–129, 1987, doi: 10.1109/jqe.1987.1073206.

[5] C. Zhao, G. Li, Y. Liu E. Gao, and X. Liu, "Silicon on insulator mach–zehnder waveguide interferometers operating at 1.3 μm," *Applied Physics Letters*, vol. 67, no. 17, pp. 2448–2449, 1995, doi: 10.1063/1.114603.

[6] H. P. Schriemer and M. Cada, "Modal birefringence and power density distribution in strained buried-core square waveguides," *IEEE Journal of Quantum Electronics*, vol. 40, no. 8, pp. 1131–1139, 2004, doi: 10.1109/jqe.2004.831641.

[7] W. N. Ye *et al.*, "Birefringence control using stress engineering in silicon-on-insulator (SOI) waveguides," *Journal of Lightwave Technology*, vol. 23, no. 3, pp. 1308–1318, 2005, doi: 10.1109/JLT.2005.843518.

[8] W. Ye, "Stress engineering for polarization control in silicon-on-insulator waveguides and its applications in novel passive polarization splitters/filters," PhD Thesis, Ottawa-Carleton Institute for Electrical Engineering, 2006.

[9] K. Okamoto, *Fundamentals of optical waveguide*. Amsterdam; Boston: Elseiver, 2006.

[10] J. A. Stratton, *Electromagnetic theory*. New York: McGraw-Hill, 1941.

[11] A. Tarraf, J. Daleiden, S. Irmer, D. Prasai, and H. Hillmer, "Stress investigation of PECVD dielectric layers for advanced optical MEMS," *Journal of Micromechanics and Microengineering*, vol. 14, no. 3, pp. 317–323, 2003, doi: 10.1088/0960-1317/14/3/001.

[12] K. Lizuka, *Elements of photonics*. Electronically Published: Wiley-Interscience, 2002.

[13] A. Yairv and P. Yeh, *Optical waves in crystals: Propagation and control of Laser Radiation*. Electronically Published: Wiley, 2003.

[14] L. Pavesi and D. Lockwood, *Silicon Photonics*. Electronically Published: Springer, 2004.

[15] L. Vivien, S. Laval, S. Dumont B. Lardenois, A. Koster, and E. Cassan, "Stress investigation of PECVD dielectric layers for advanced optical MEMS," *Optics Communications*, vol. 210, no. 1–2, pp. 43–49, 2002, doi: 10.1016/s0030-4018(02)01681-4.

[16] D.-X. Xu *et al.*, "Design of polarization-insensitive components using geometrical and stress-induced birefringence in SOI waveguides," *SPIE Proceedings*, vol. 5730, pp. 158–172, 2005, doi: 10.1117/12.589158.

[17] M. Huang, "Stress effects on the performance of optical waveguides," *Inter. J. Solids and Structures*, vol. 40, no. 7, pp. 1615–1632, 2003, doi: 10.1016/s0020-7683(03)00037-4.

[18] J. Xu and R. Stroud, *Acousto-optic devices: Principles, design, and applications*. -: Wiley, 1992.

[19] Y. S. Chen and H. Fatemi, "Stress measurements on multilevel thin film dielectric layers used in Si integrated circuits," *J. Vac. Sci. Technol. A*, vol. 4, pp. 645–649, 1986.

[20] T. M. J, C. R. W, H. C. Martin, and L. J. Topp, "Stiffness and deflection analysis of complex structures," *Journal of the Aeronautical Sciences*, vol. 23, no. 9, pp. 805–823, 1956, doi: 10.2514/8.3664.

[21] O. C. Zienkiewicz, *The Finite Element Method in engineering science*. -: McGraw-Hill, 1971.

[22] S. Timoshenko and J. N. Goodier, *Theory of Elasticity*. New York: McGraw-Hill, 1951.